Complex spin structure and magnetic phase transition of Mn3−xFexSn alloys

Hanggai, W.; Hamutu, O.; de Wijs, G. A.; Dugulan, I.; van Dijk, N. H.; Brück, E.

DOI
10.1103/pvjm-jvsr

Publication date
2025

Document Version
Final published version

Published in
Physical Review B

Citation (APA)
Hanggai, W., Hamutu, O., de Wijs, G. A., Dugulan, I., van Dijk, N. H., & Brück, E. (2025). Complex spin structure and magnetic phase transition of Mn3−xFexSn alloys. *Physical Review B*, *112*(1), 14407-1-14407-15. https://doi.org/10.1103/pvjm-jvsr

PHYSICAL REVIEW B **112**, 014407 (2025)

Complex spin structure and magnetic phase transition of $Mn_{3-x}Fe_xSn$ alloys

W. Hanggai[1,*] O. Hamutu,[1] G. A. de Wijs,[2] I. Dugulan,[1] N. H. van Dijk,[1] and E. Brück[1]
[1]*Fundamental Aspects of Materials and Energy (FAME), Faculty of Applied Sciences,*
Delft University of Technology, Mekelweg 15, 2629JB Delft, The Netherlands
[2]*Radboud University, Institute for Molecules and Materials, Heyendaalseweg 135, 6525AJ Nijmegen, The Netherlands*

(Received 20 September 2024; revised 6 February 2025; accepted 21 May 2025; published 7 July 2025)

The hexagonal $Mn_{3-x}Fe_xSn$ compounds possess several desirable properties that make them suitable magnetocaloric materials, including a ferromagnetic (FM)-to-paramagnetic (PM) transition near room temperature and soft magnetic behavior. In this study, we use the melt-spinning technique to explore the Mn-Fe-Sn ternary system. By combining magnetization measurements, Mössbauer spectroscopy, neutron diffraction (ND), oriented powder x-ray diffraction, and density functional theory (DFT) calculation, the magnetocaloric effect, spin structures, and the intrinsic magnetic properties of polycrystalline $Mn_{3-x}Fe_xSn$ ($x = 0.8 - 1.4$) compounds are determined. The FM-to-PM transition temperature T_C ranges from 253 K ($x = 0.8$) to 394 K ($x = 1.4$). At low temperature, a spin reorientation at T_S is observed, where below T_S a coexistence of FM order with spins along the c axis and antiferromagnetic order with spins within the $a - b$ plane occurs for $x = 0.8$ and 1.0. However, for compounds with $x = 1.2$ and 1.4, only FM order with spins along the c axis has been found below T_S. Above T_S, the spin structure corresponds to FM order with spins aligned within the $a - b$ plane for all compositions. The magnetic moments of Mn and Fe were evaluated using DFT, demonstrating good agreement with the ND results.

DOI: 10.1103/pvjm-jvsr

I. INTRODUCTION

The investigation and utilization of Heusler alloys have attracted increasing attention due to their fascinating physical properties and potential applications as giant magnetocaloric effect (MCE) materials [1–3], ferromagnetic (FM) shape-memory alloys [4–6], topological insulators [7], and half-metals [8,9]. The X_2YZ compounds, where X and Y are 3d transition metals and rare-earth metals and Z is a main group element (like Si, Al, Ge, Ga, Sn, and Sb), manifest diverse crystalline symmetries, such as cubic, tetragonal, and hexagonal [10,11]. Since the rare-earth crisis of 2011, persistent supply-chain vulnerabilities, and price fluctuations of rare-earth metals, there has been growing research interest in the development of rare-earth-free materials for various applications [12,13]. Hence, Sn-based Mn-Fe-Sn alloys offer markedly superior properties than commercially available alternatives, with the added benefits of good availability and sustainability [14]. Properties like sizeable magnetocrystalline anisotropy, a high spin polarization, and high transition temperatures qualify them as good candidates for magnetic materials with high performance for spintronics [15–17]. Subsequently, density functional theory (DFT) calculations predicted that the Heusler alloy (Mn, Fe)$_3$Sn is a promising MCE material for magnetic heat pump and thermomagnetic motor applications [18–24]. Due to their relatively high magnetic moments and transition temperatures, they can be adjusted continuously by their Mn/Fe ratio [14]. According to the binary Mn-Sn and Fe-Sn phase diagrams, the Mn Sn and Fe_3Sn compounds both crystallize in the hexagonal Mg_3Cd-type structure [25–28]. However, the processing route for these two compounds requires a different heat treatment. The Mg_3Cd-type crystal structure with $P6_3/mmc$ symmetry (space group 194) is composed of two layers, each containing three magnetic (Mn, Fe) atoms at the 6h site and one nonmagnetic Sn atom at the 2d site of the hexagonal unit cell [29,30]. The magnetic atoms are arranged in a triangle in each layer [29].

Authors of previous studies on the Sn-based Mn-Fe-Sn system have identified several different applications based on their different intrinsic properties. Neutron diffraction (ND) studies of Mn_3Sn [25,31–43] have revealed an inverse antiferromagnetic (AFM) triangular spin structure below $T_N \approx$ 420 K [30,35]. It is proposed that these properties enable promising applications in data storage high-density memory integration and ultrafast data processing [15] due to the insensitivity of AFM spin structures to perturbations, the absence of stray fields, and fast spin dynamics [44,45]. However, a single crystal of Mn_3Sn measured in an applied magnetic field oriented along $\mathbf{H} \parallel (0\ 1\ 0)$ revealed the presence of weak FM with hysteresis at $T = 300$ K [30]. Authors of polarized ND studies elucidated that the weak FM observed in Mn_3Sn originates from the triangular AFM structure itself. This phenomenon is attributed to the change in orientation

---

[*] Contact author: H.Gai@tudelft.nl

induced by the interaction between the magnetic field and the FM moment, which varies depending on the orientation of the triangular AFM structure [35,42,46]. On the other side, the nature of FM ordering in the Fe_3Sn compound [27,47–49] has been examined for permanent magnetic applications, revealing a high Curie temperature ($T_C \approx 725$ K), a basal plane magnetic anisotropy constant of 1.8 $\mathrm{MJ\,m^{-3}}$, and a sizeable magnetization $M_s = 120\,\mathrm{Am^2\,kg^{-1}}$ at room temperature [27,28,49–52]. While the magnetocrystalline anisotropy corresponds to the easy plane, its considerable absolute value has led to investigations into potential modifications aimed at shifting the anisotropy from the easy plane to the easy axis [53]. Subsequently, theoretical calculations predicted that tuning the anisotropy from the easy plane to the easy axis is feasible by replacing Sn with Sb [49,54]. For the above compounds, both experimental studies and DFT calculations were employed to evaluate the magnitude of the magnetic moments on the 6*h* site. DFT calculations yielded a magnetic moment of ~3.0 μ_B/Mn for Mn_3Sn [34,35,43,55] and 2.4 μ_B/Fe for Fe_3Sn. However, previous experimental results for the Mn_3Sn compound exhibited slightly lower magnetic moments, ranging from 2.1 to 2.75 μ_B/Mn [33,56,57]. Later, Brown *et al.* [35] and Cable *et al.* [37] presented experimental values closer to the theoretical prediction of ~3.0 μ_B/Mn for Mn_3Sn. For Fe_3Sn, the calculated saturation magnetization of 2.4 μ_B/Fe is slightly higher than the experimental value of 2.2 μ_B/Fe at 10 K [27,49,54]. This difference is attributed to the 4*s* electrons that, in metallic iron, are negatively polarized by ~0.2 μ_B per atom, with respect to the 3*d* electrons. Therefore, experimental results suggest that the atomic moment of iron metal 2.2 μ_B/Fe would be composed of ~2.4 μ_B/Fe from the 3*d* electrons and $\sim -0.2\mu_B$/Fe from the 4*s* electrons [50].

The characteristics of the these compounds are not suitable for applications in magnetic heat pumps or thermomagnetic motors, as they require a significant MCE centered around a Curie temperature near room temperature. Hence, a transition temperature (T_C) that is tunable near room temperature is required for magnetocaloric materials (MCMs) in magnetic heat pump applications. This is achievable by switching from binary Mn-Sn and Fe-Sn to ternary Mn-Fe-Sn alloys by partially replacing Mn by Fe [14]. When in Mn_3Sn $\frac{1}{3}$ of the Mn is replaced by Fe, the transition temperature of Mn_2FeSn is shifted to a value near room temperature. The magnetic moments that were originally lying on a kagome lattice for Mn_3Sn will be broken in Mn_2FeSn by a rearrangement of the spin structure. The rearrangement of the magnetic moments has the potential to generate new spin configurations [54]. The FM interaction in the Mn_2FeSn compound is enhanced, and as a result, the magnetic structure changes [58,59]. Hence, the FM-to-paramagnetic (PM) transition in $Mn_{3-x}Fe_xSn$ alloys holds the potential to generate promising MCEs. The spin configuration of Mn_2FeSn and complex magnetic structure evolution with temperature have not yet been resolved. Therefore, the influence of the Mn/Fe ratio on the magnetic properties of $Mn_{3-x}Fe_xSn$ alloys constitutes the primary focus of this study. In this article, we combine magnetization measurements, x-ray diffraction (XRD), Mössbauer spectroscopy, neutron powder diffraction, and DFT calculations to investigate the MCE and the structural and magnetic properties of $Mn_{3-x}Fe_xSn$ ($x = 0.8 - 1.4$) alloys.

II. EXPERIMENTAL AND CALCULATION METHODS

High-quality polycrystalline $Mn_{3-x}Fe_xSn$ alloys with x ranging between 0.8 and 1.4 were prepared by the traditional arc-melting method in a high-purity argon atmosphere. Elemental starting materials with a purity of 99.9% for Mn, Fe, and Sn were weighted in terms of the stoichiometric amount. Here, 2 wt. % excess Mn was added to compensate for weight loss during melting. Homogeneity for the sample of 5 g was ensured by turning and remelting five times. Evaporation was found to vary between 1.05 and 2.05 wt. %. Then the as-cast ingots were melted and quenched by melt spinning with a copper-wheel speed of $v \approx 30$ m/s. The melt-spun ribbons with a width of 2–3 mm and thickness of 15–25 μm were produced. To ensure the phase homogeneity, the $Mn_{3-x}Fe_xSn$ compounds were sealed in a quartz tube filled with a high-purity argon atmosphere. Finally, the samples were annealed at 500 °C for 2 h and then quenched in cold water.

The crystalline structure and phase composition of the polycrystalline samples were evaluated using powder XRD, and scanning electron microscopy (SEM, JEOL JSM 6500 F, Japan) coupled with energy-disperse x-ray spectroscopy (EDS). XRD was carried out on a PANalytical X-Pert PRO diffractometer, using Cu-$K\alpha$ radiation 1.5405 Å (angular range 10°–90°, angular step 0.02°, 1 s per step). The samples were placed on a spinner to limit preferential crystalline orientation. ND experiments were carried out at the research reactor of the TU Delft [60]. A neutron wavelength of 1.67 Å was selected by the (5 3 3) reflection of a germanium single-crystal monochromator. Data were collected at temperatures of 5, 80, 250, and 500 K. Refinements of x-ray and ND data were analyzed by the Rietveld method [61], as implemented in the FULLPROF suite [62]. The temperature- and field-dependent magnetization was measured with a superconducting quantum interference device (SQUID, Quantum Design MPMS XL) magnetometer, using the reciprocating sample option mode. Magnetization in the temperature range from 5 to 370 K was collected at a constant sweep rate of 2 K/min and in applied magnetic fields up to 2 T. Additional magnetic hysteresis loops were measured at different temperatures in magnetic fields ranging from −5 to 5 T. Magnetic measurements at temperatures >370 K were performed in a VersaLab vibrating-sample magnetometer with an oven function. Field-oriented samples were embedded in epoxy glue and oriented with an applied magnetic field of $\mu_0 H = 1$ T in the FM state. Prior to orienting in field, the samples were hand-milled and then sieved down to a powder size <10 μm. Transmission ^{57}Fe Mössbauer spectra were collected at different temperatures with a conventional constant-acceleration spectrometer using a ^{57}Co (Rh) source. Velocity calibration was carried out using an α-Fe foil at room temperature. Mössbauer spectra were fitted using the Mosswinn 4.0 program [63].

DFT calculations were carried out with VASP [64] using the Perdew-Burke-Ernzerhof exchange-correlation functional [65,66] and the projector augmented-wave (PAW) method [67,68]. To establish trends in total energy and net magnetic moment without using supercells, calculations were carried out using the virtual crystal approximation (VCA) with special PAW datasets. These datasets were constructed inspired

TABLE I. Lattice parameters a and c, c/a ratio, and unit-cell volume V obtained by room-temperature XRD, phase fractions, saturation magnetization M_s, and Curie temperature T_C for the $Mn_{3-x}Fe_xSn$ ($0.8 \leqslant x \leqslant 1.4$) compounds. M_s is obtained from magnetization measurements at 5 K and the transition temperatures T_C defined as the minimum in dM/dT in an applied field of 0.01 T.

x	a (Å)	c (Å)	c/a	V (Å^3)	Main wt. (%)	Impurity wt. (%)	$M_{s,5\,K@5\,T}$ (Am^2 kg^{-1})	T_C (K)
0.8	5.58989(7)	4.46896(6)	0.79947(1)	120.933(3)	98.7(6)	1.3(1)	64.27	253
0.9	5.57903(8)	4.46021(7)	0.79946(2)	120.227(3)	98.3(5)	1.7(1)	70.25	272
1.0	5.5695(1)	4.45097(1)	0.79917(2)	119.569(4)	98.2(7)	1.8(1)	76.47	305
1.1	5.56233(7)	4.44581(6)	0.79927(1)	119.123(3)	97.9(5)	2.1(2)	82.64	325
1.2	5.55709(7)	4.43921(6)	0.79884(1)	118.722(3)	97.7(6)	2.3(2)	86.42	351
1.3	5.54841(7)	4.43167(6)	0.79873(1)	118.151(3)	97.9(6)	2.1(2)	92.26	371
1.4	5.5447(1)	4.42473(9)	0.79800(2)	117.811(3)	98.2(7)	1.8(2)	95.48	394

by the *GW*-style datasets for Mn and Fe with frozen [Ne] core from the VASP distribution. They interpolate, using fractional charges, between Mn ($Z = 15$ effective core charge) and Fe ($Z = 16$ effective core charge) and were generated for $Z =$ 15, 15.11, 15.17, 15.23, 15.33, 15.67, and 16, keeping the different potentials as similar as possible. For Sn, the standard potential with frozen [Kr] core was used.

Calculations were done in a primitive hexagonal cell with eight atoms that was fully optimized (c, a, internal coordinates) observing only symmetry requirements. The kinetic energy cutoff was 600 eV, and a Γ-centered 7 × 7 × 10 **k**-point mesh with Methfessel-Paxton smearing of first order ($\sigma = 0.1$ eV) was employed [69]. Spin-orbit coupling was used with two-component spinors [70,71].

To obtain more realistic models on Mn_2FeSn, some calculations were carried out without VCA. For these, we used the same potentials with $Z = 15$ (Mn) and $Z = 16$ (Fe). A few checks were carried out, repeating some calculations with potentials of the standard VASP 54 distribution. We used the same cutoff and smearing as for VCA. Fixed hexagonal lattice parameters were $a = 5.57$ Å and $c = 4.45$ Å (cf. Table I). Fe and Mn were positioned randomly at the 6h sites in a 2 × 2 × 1 super cell ($a = 11.13$ Å and $c = 4.45$ Å). Internal coordinates were optimized using both 2 × 2 × 4 and, in the final optimization steps for the canted magnetic structure, 4 × 4 × 10 Γ-centered **k**-point meshes. The densities of states (DOSs) were obtained with the Γ-centered 4 × 4 × 10 **k**-point mesh using the tetrahedron method [72].

III. RESULTS AND DISCUSSION

A. Crystalline structure

The room-temperature XRD refinements at ambient temperature confirm that the $Mn_{3-x}Fe_xSn$ ($x = 0.8 - 1.4$) compounds all crystallize in the Mg_3Cd-type hexagonal structure with space group $P6_3/mmc$ (194). The Mn and Fe atoms share the Wyckoff positions of the 6h site, while the Sn atoms occupy the 2d site. This result agrees with those for other Sn-based Mn_3Sn and Fe_3Sn compounds [14,49,51]. Figure 1(a) shows the Rietveld refinement results for the polycrystalline Mn_2FeSn compound. All diffraction peaks marked with their crystal plane index can be identified as the Mg_3Cd-type hexagonal structure with a minor secondary phase. According to literature reports, compounds prepared by traditional arc-melting methods show texture [58,59]. However, the compounds prepared by melt-spinning do not exhibit a preferred crystallographic orientation in the Rietveld refinement results.

To identify the impurity phase and examine the microstructure of the $Mn_{3-x}Fe_xSn$ compound, SEM imaging coupled with EDS chemical analyses unveiled coexistence of $Mn_{3-x}Fe_xSn$ and $Mn_{1.75-x}Fe_xSn$ phases in the Mn_2FeSn compound. The inset in Fig. 1(a) shows the backscattered electron image of the Mn_2FeSn compound. Obvious contrast can be seen, where the gray region is the Mg_3Cd-type main phase and the light gray area represents the compositional segregation of the Sn-rich phase $Mn_{1.75-x}Fe_xSn$, which is identified as the $Mn_{1.75}Sn$-type hexagonal structure (space group $P6_3/mmc$). This is in good agreement with the results reported by Felez *et al.* [14] and Liu *et al.* [59]. Furthermore, the grain size and grain boundaries of the compounds are clearly visible in the inset of Fig. 1(a). This is because Sn tends to segregate to grain boundaries [73,74]. It was found that the impurity phase preferentially occupies the grain boundaries. When the grains of the main phase in samples with $x = 0.8$ and 1.4 are compared, a clear trend can be observed. Specifically, the $x = 0.8$ sample exhibits a log-normal distribution with an average grain size in the range of 3–4 μm. An increase in Fe content to $x = 1.4$ causes an increase in average grain size to 7–8 μm, as shown in Fig. S1 in the Supplemental Material [75]. For the grain size evaluation, ∼15 SEM images per samples were analyzed using MIPAR software [76] to obtain a quantitative estimate of the average grain size. Compared with other MnNi-X-Y (X = Co, Fe; Y = Sn, In)-based Heusler alloys, this grain size is significantly smaller [77–80].

The weight fractions of the main and impurity phases in the $Mn_{3-x}Fe_xSn$ compounds are shown in Fig. 1(b) and Table I. For $0.8 \leqslant x \leqslant 1.4$, the impurity phase was 1–2 wt. %. In our experimental results, the ratio of Mn : Fe = 1.6:1.4 is the limit for Mn/Fe substitution at 500 °C. This is because, according to the binary Mn-Sn phase diagram, the Mn_3Sn phase is stable at 500 °C [26], and according to the binary Fe-Sn phase diagram, the Fe_3Sn phase is stable in a temperature range of 750–1080 °C [10,52,59]. Meanwhile, it is reasonable to assume that a further increase in the Fe/Mn ratio for the $Mn_{3-x}Fe_xSn$ compounds will lead to an increase in annealing temperature up to 800 °C [10,52]. Figures 1(c) and 1(d) and Table I show the refined lattice parameters and the unit-cell volume. By replacing Mn by Fe, the lattice parameters a and c and the unit-cell volume V decrease linearly. In general, Fe substitution for Mn leads to a contraction of the unit cell with

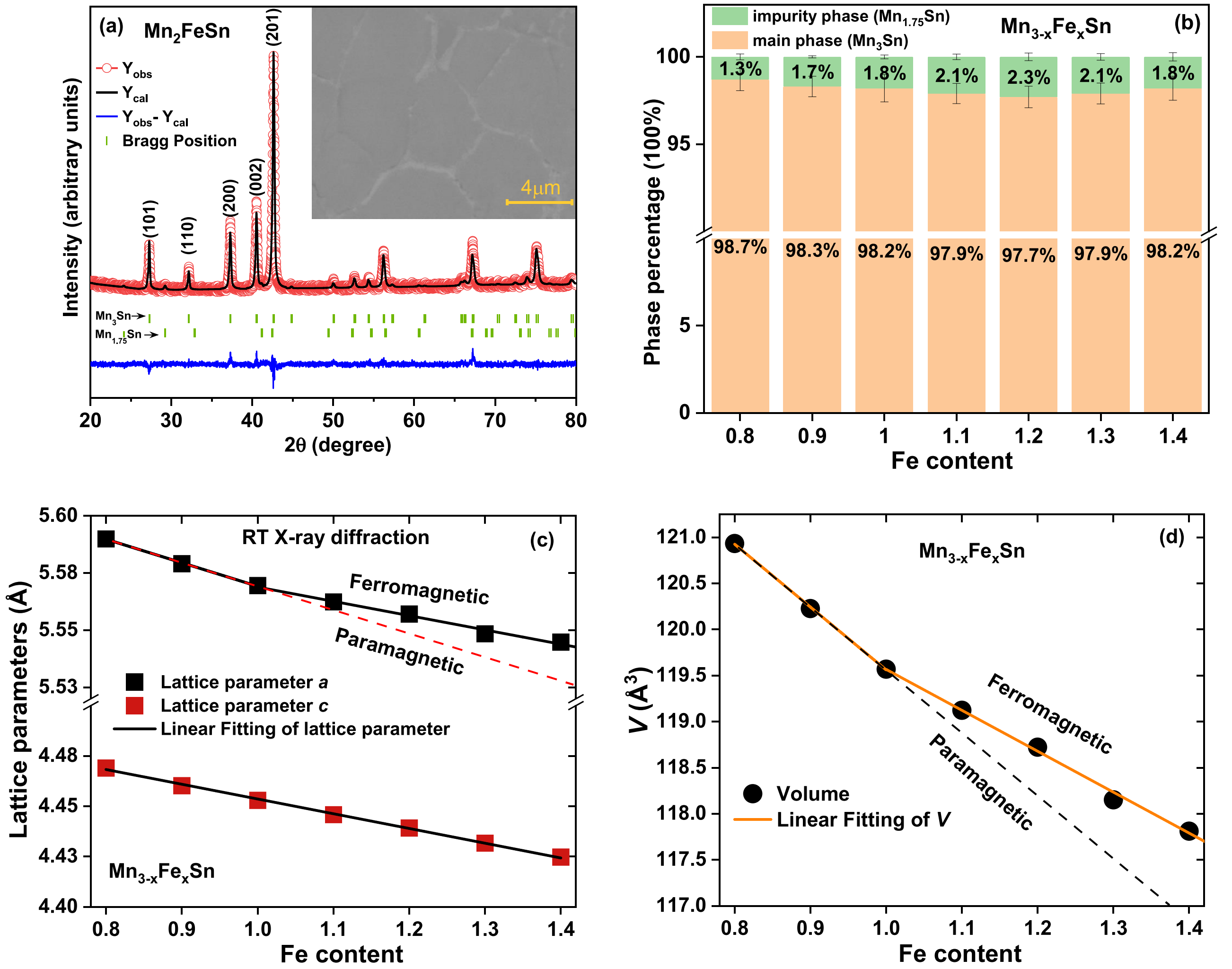

FIG. 1. (a) Refined x-ray diffraction (XRD) pattern for the Mn_2FeSn compound. The inset shows the backscattered electron image of the Mn_2FeSn compound. (b) Phase fraction (wt. %) for the $Mn_{3-x}Fe_xSn$ alloys. (c) Lattice parameter a and c of $(Mn,\ Fe)_3Sn$ ($x = 0.8 - 1.4$). (d) Unit-cell volume V of $(Mn,\ Fe)_3Sn$ ($x = 0.8 - 1.4$).

a decrease in both hexagonal lattice parameters because the atomic radius of Fe is smaller than that of Mn. The linear change in lattice parameter a and volume V exhibits a kink at the transition from the PM to the FM state because of the magnetovolume contribution. In contrast, the lattice parameter c exhibits continuously a linear change, which most likely indicates that the magnetic moments are aligned within the $a - b$ plane at room temperature.

B. Magnetic phase transition

To understand the magnetic properties of the $Mn_{3-x}Fe_xSn$ ($x = 0.8 - 1.4$) compounds, the temperature dependence of magnetization is measured, employing zero-field-cooled (ZFC) and field-cooled (FC) modes from 5 to 370 K under a magnetic field of 1 T, as shown in Fig. 2(a). The ZFC (lower curve) and FC (upper curve) magnetization curves for samples with $0.8 \leqslant x \leqslant 1.4$ do not overlap at low temperatures, indicating magnetic anisotropy. The *M-T* curves for heating and cooling coincide without thermal hysteresis. This suggests that these compounds show a second-order phase transition (SOPT) at T_C. Figure 2(b) shows the FC magnetization vs temperature (*M-T*) curves recorded at temperatures from 370 to 5 K under an applied field of 0.01 T for $Mn_{3-x}Fe_xSn$ ($x = 0.8 - 1.1$) compounds, two distinct magnetic transitions are evident in this material system. One transition occurs at higher temperatures, marking the transition from the PM to the FM state. The Curie temperature defined as the minimum of dM/dT in a field of 0.01T is shown in the inset of Fig. 2(b). Additionally, a low-temperature feature is observed in Fig. 2(b), which indicates a spin-reorientation transition or the formation of a complex AFM state, which is incompatible with a collinear FM arrangement. This structure can easily evolve into FM at intermediate magnetic fields [58,59].

Figure 2(c) shows the systematically recorded M-μ_0H magnetization vs magnetic field for the free-powder polycrystalline samples, showing data for the most representative temperature of 5 K. The measurements were performed along five quadrants and point toward a soft FM behavior with a small magnetic hysteresis loop. For instance, the $x = 1.4$ compound shows the highest coercive field of $\mu_0H_C = 18$ mT and remnant magnetization $M_{rem} = 9.87\ \mathrm{Am^2\,kg^{-1}}$ at 5 K,

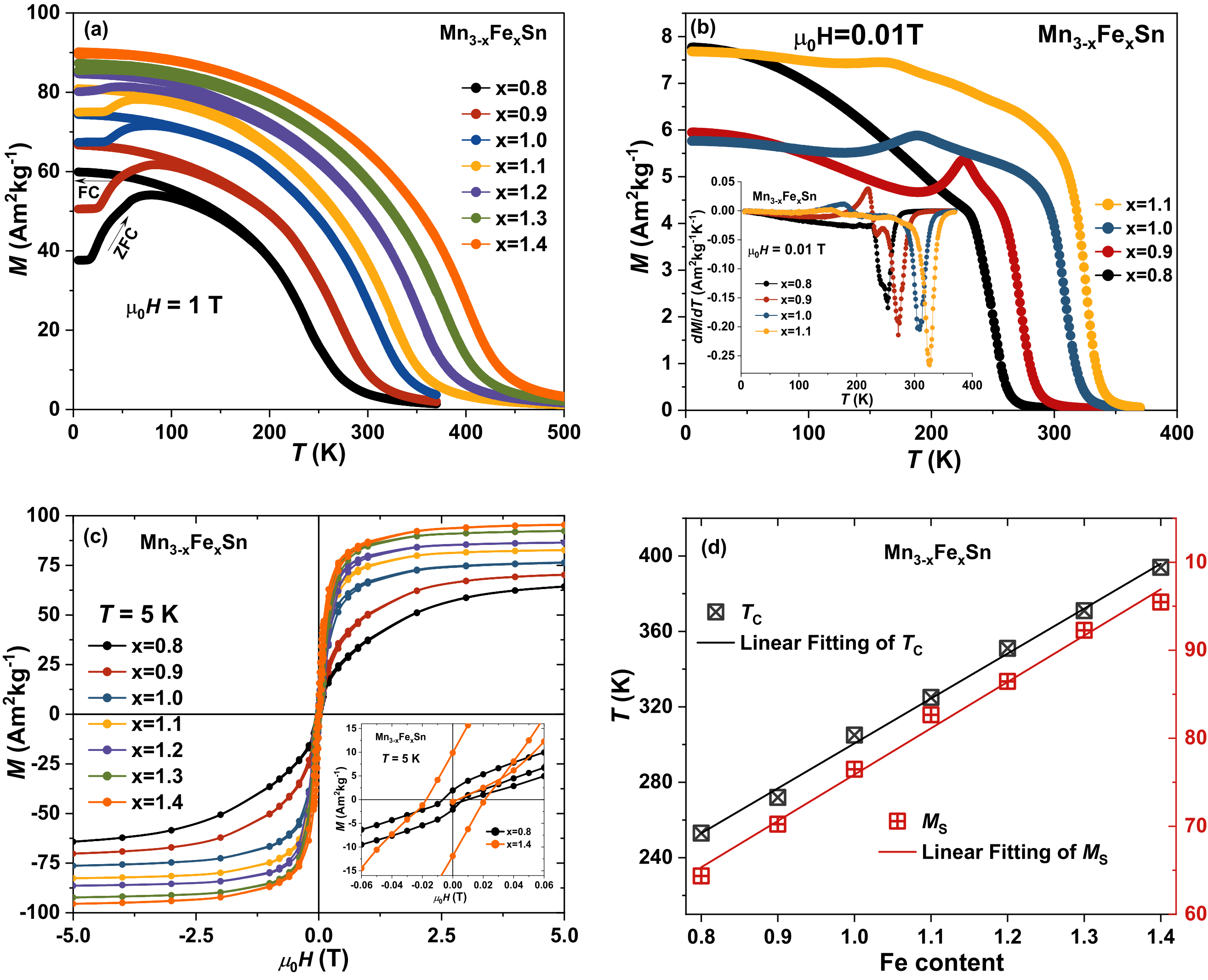

FIG. 2. (a) Magnetization as a function of temperature in an applied field of 1 T and (b) magnetization vs temperature in an applied field of 0.01 T. The inset shows the *dM*/*dT* curves in a field of 0.01 T for $x = 0.8 - 1.1$. (c) Magnetization as a function of magnetic field of Mn$_{3-x}$Fe$_x$Sn ($0.8 \leqslant x \leqslant 1.4$) at 5 K. The inset shows a zoomed part of the magnetic hysteresis loop of Mn$_{3-x}$Fe$_x$Sn ($x = 0.8$ and 1.4). (d) Values of T_C and M_s for the Mn$_{3-x}$Fe$_x$Sn ($0.8 \leqslant x \leqslant 1.4$) compounds as a function of the Fe content.

as shown in the inset of Fig. 2(c). The magnetic saturation is effectively reached at 2 T for $1.1 \leqslant x \leqslant 1.4$. This agrees with the field-dependent magnetization results reported by Felez *et al.* [14] for Mn$_{3-x}$Fe$_x$Sn compounds. One can note that, for $x = 0.8$, 0.9, and 1.0, the field-dependent magnetization measurements at 5 K show ferrimagnetic behavior without saturation for fields up to 5 T. This indicates that the magnetic moments are sizeable and most likely have an AFM component. In previous studies of the polycrystalline Mn-Fe-Sn system, observation of the coexistence of FM and AFM phases is not uncommon [58,81–83], which we will discuss in the next section. Figure 2(d) shows the linear correlation between the saturation magnetization and transition temperature. In the Mn$_{3-x}$Fe$_x$Sn ($x = 0.8$-1.4) compounds, the transition temperature can be varied continuously in the temperature range from 250 to 396 K by adjusting the Mn/Fe ratio. This satisfies a crucial requirement for the application of MCMs, ensuring that the transition temperature can be adjusted continuously across the temperature range required for magnetic heat pump applications, particularly considering the finite MCE centered around the Curie temperature. As shown in Fig. S2 in the Supplemental Material [75] and Table II, the saturation magnetizations (M_s) in a field of 7 T for Mn$_{2.2}$Fe$_{0.8}$Sn and Mn$_{1.6}$Fe$_{1.4}$Sn correspond to 69.96 and 95.98 Am^2 kg^{-1}, respectively. These values for the saturation magnetization are comparable with those of most existing MCMs [80,84–86].

The magnetocaloric performance expressed as the isothermal entropy change ΔS_m is shown in Fig. 3(a). The isothermal magnetic entropy change is calculated by applying the Maxwell relation $\Delta S_m(T)_{\Delta H} = \int_{Hi}^{H_f} \mu_0 [\frac{\partial M(T,H)}{\partial T}]_H \, dH$ [87,88] to the isofield *M*(*T*) data. The magnetic or indirect calorimetric determinations of the magnetic entropy change suffer from uncertainties, typically of the order of 10% [89]. The maximum values in magnetic entropy change (ΔS_m) measured for the Mn$_{3-x}$Fe$_x$Sn ($x = 0.8$, 1.0, 1.2, and 1.4)

TABLE II. Calculated $|\Delta S_{\mathrm{m,max}}|$ for $\mathrm{Mn}_{3-x}\mathrm{Fe}_x\mathrm{Sn}$ ($x = 0.8$, 1.0, 1.2, 1.4) in a field change of 2 T. The magnetic moment per formula unit derived from the SQUID measurements in a maximum applied magnetic field of $\mu_0 H = 7$ T at 5 and 80 K. The magnetic moment per atom/formula unit of the FM and AFM structures were calculated from neutron powder diffraction data at 5 and 80 K.

		$M_{\mathrm{s,7\,T}}$ (μ_B/f.u.)		FM (μ_B/f.u.)		AFM (μ_B/f.u.)		FM (μ_B/atom)		AFM (μ_B/atom)	
x	$\Delta S_{\mathrm{m,max}}$ (J kg^{-1} K^{-1})	5 K	80 K	5 K	80 K	5 K	80 K	5 K	80 K	5 K	80 K
0.8	1.10	3.59(1)	3.49(2)	3.86(13)	3.83(13)	6.67(10)	6.32(10)	1.29(7)	1.28(7)	2.23(5)	2.11(5)
1.0	1.18	4.02(1)	3.94(1)	4.18(9)	4.11(9)	5.71(6)	5.40(6)	1.40(5)	1.37(5)	1.91(3)	1.80(4)
1.2	1.40	4.39(1)	4.33(1)	4.50(10)	4.48(10)	—	—	1.50(6)	1.49(6)	—	—
1.4	1.41	4.77(1)	4.73(1)	5.05(10)	4.95(9)	—	—	1.68(6)	1.65(5)	—	—

compounds are shown in Table II. It is evident that the increase in Fe content from 0.8 to 1.4 results in a 30% enhancement in $|\Delta S_m|$, with the maximum value of $|\Delta S_m|$ from 1.10 to 1.41 J kg^{-1} K^{-1} for a magnetic field change of 2 T. Unlike first-order phase transition (FOPT) materials, the observed magnetic entropy change is relatively low, which is typical for SOPT materials. To qualitatively evaluate the order of the magnetic phase transition in $\mathrm{Mn}_{3-x}\mathrm{Fe}_x\mathrm{Sn}$ materials, the field dependence of the isothermal magnetic entropy change with power-law behavior of the type $|\Delta S_{\mathrm{m}}| \propto H^n$ is evaluated [90,91]. The field exponent n can be used to classify the nature of the magnetic order: FOPT or SOPT. The field exponent $n = \frac{d\ln(|\Delta S_{\mathrm{m}}|)}{d\ln(H)}$ for the magnetic entropy change as a function of magnetic field is evaluated. In Fig. 3(b), the high-temperature limit $n \approx 2$ and the low-temperature limit $n \approx 1$ are clearly depicted [92]. When the FM-to-PM phase transition is crossed, the minimum value for the exponent corresponds to the value predicted for the SOPT of $n_{\min} = \frac{2}{3}$ and a maximum value of $n_{\max} \leqslant 2$ is obtained [92], which is also a characteristic feature for the SOPT. Figure 3(b) shows clearly that the field exponents are restricted by the high-temperature value as an upper limit: $n_{\max} < 2$ near T_{C}. Similar results were obtained for other magnetic field change values. Not only the $n_{\max}$ values but also their temperature evolution and $n_{\min} \approx \frac{2}{3}$ are typical for materials with a SOPT [91]. This is consistent with the absence of thermal hysteresis in the $M(T)$ curves for these materials.

C. Magnetic structure

The spin configurations of intermediate $\mathrm{Mn}_{3-x}\mathrm{Fe}_x\mathrm{Sn}$ compositions, probably influenced by the crossover in magnetic behavior from $\mathrm{Mn}_3\mathrm{Sn}$ (AFM) to $\mathrm{Fe}_3\mathrm{Sn}$ (FM), have not been studied as a function of Fe/Mn ratio. While $\mathrm{Mn}_3\mathrm{Sn}$ shows AFM ordering (with spins within the $a - b$ plane) [30], $\mathrm{Fe}_3\mathrm{Sn}$ exhibits FM ordering (with spins along the a axis) [27,52]. To qualitatively investigate the evolution of the magnetic structure from AFM to FM order for an increasing Fe/Mn ratio, we examined a series of representative compositions within the $\mathrm{Mn}_{3-x}\mathrm{Fe}_x\mathrm{Sn}$ ($x = 0.8$, 1.0, 1.2, and 1.4) compounds by powder ND measurements. ND is a powerful technique to investigate the crystalline structure and magnetic properties of materials, with sensitivity to the size and orientation of magnetic moments, thereby providing the ability to resolve the magnetic structure. This makes ND an essential tool for studying magnetic materials and investigating magnetic phase transitions. Hence, ND was carried out on $\mathrm{Mn}_2\mathrm{FeSn}$ at five different temperatures (5, 80, 250, 298, and 500 K). These temperatures were selected based on magnetization

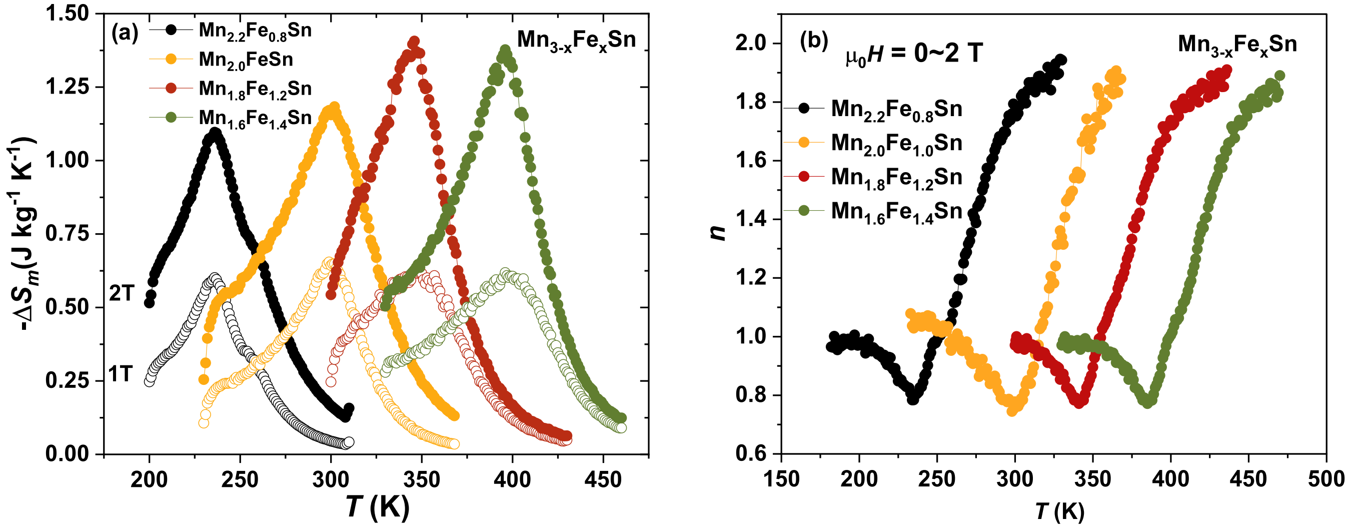

FIG. 3. (a) Isothermal entropy change $-\Delta S_m$ from the temperature-dependent magnetization $M(T)$ upon heating in a magnetic field change of 1 T (open symbols) and 2 T (closed symbols) for the $\mathrm{Mn}_{3-x}\mathrm{Fe}_x\mathrm{Sn}$ ($x = 0.8 - 1.4$) compounds. (b) Field exponent n of the entropy change for the $\mathrm{Mn}_{3-x}\mathrm{Fe}_x\mathrm{Sn}$ ($x = 0.8 - 1.4$) compounds.

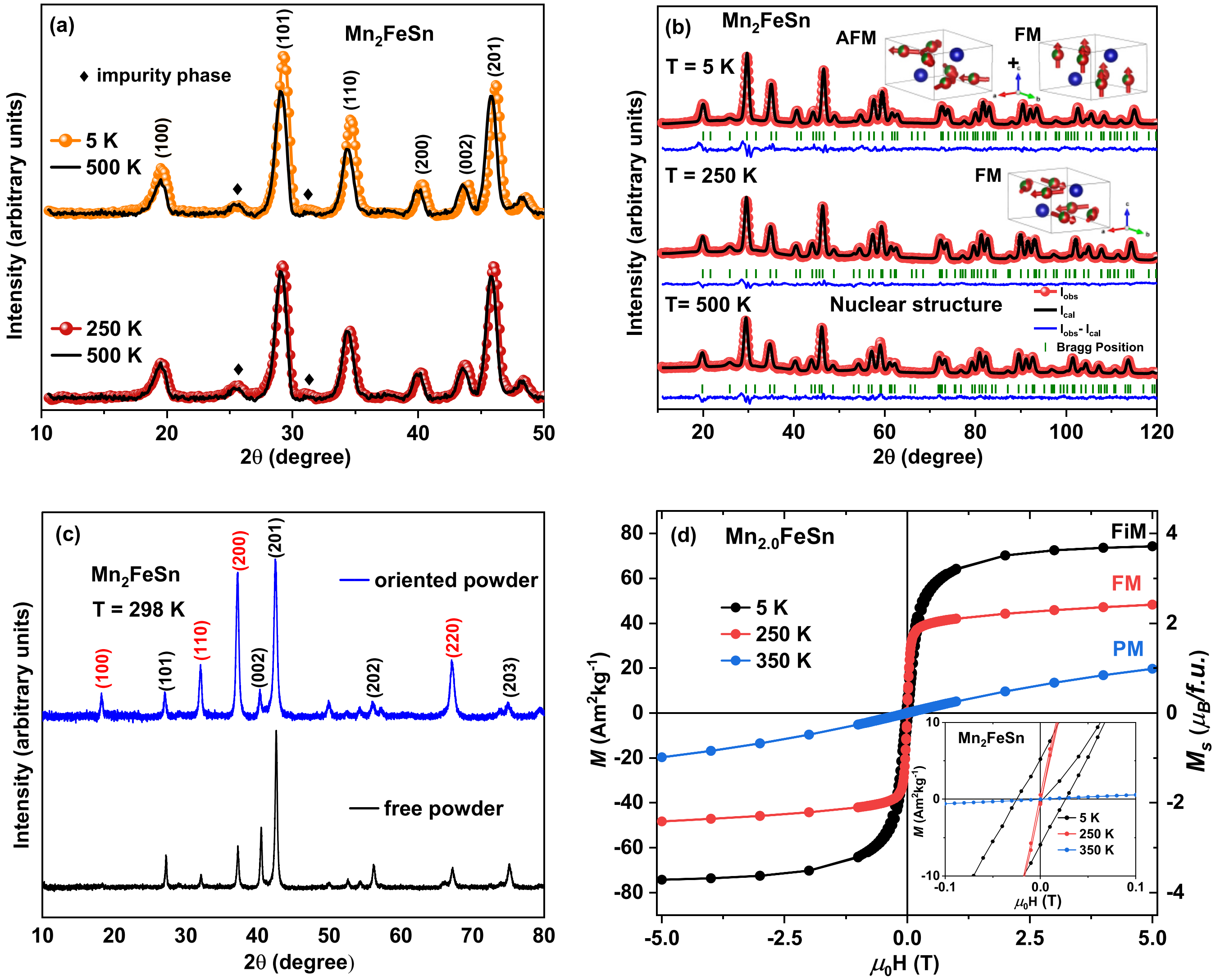

FIG. 4. (a) Powder neutron diffraction pattern of the Mn_2FeSn compound obtained at 5, 250, and 500 K. (b) Refinements of the nuclear and magnetic structure. (c) Comparison between random (bottom curve) and oriented powder (top curve) x-ray diffraction (XRD) with large changes in the indexed peak intensities. (d) Magnetization as a function of magnetic field for the Mn_2FeSn compound at 5, 250, and 350 K.

measurements in a field of 0.01 T. Figure 4(a) shows a comparison of the ND patterns for the Mn_2FeSn compound in the FM+AFM (5 K), the FM (250 K), and PM (500 K) states. No additional peaks emerge in the ordered state compared with the disordered state of Mn_2FeSn. Therefore, the propagation vector of the magnetic structure corresponds to $\mathbf{k} = (0,0,0)$. From the enhancement of the peak intensity of the (100) and (200) reflections at 5 K, it can be deduced that there is a significant magnetic spin component along the c axis, whereas the discernible magnetic contribution of the (002) peak at 250 K indicates a spin alignment within the $a-b$ plane. A symmetry operation analysis of space group 194 (hexagonal $P6_3/mmc$ symmetry) has been performed by BASIREPs (part of the Winplotr suite). Table S1 in the Supplemental Material [75] presents all possible irreducible representations and the corresponding basis vectors (Φ) for FM and AFM ordering.

The refinement of the ND patterns of Mn_2FeSn shown in Fig. 4(b) confirm the hexagonal Mg_3Cd-type hexagonal structure with space group $P6_3/mmc$ (194) for the Mn_2FeSn compound. The low-temperature lattice constants derived from ND measurements are shown in Fig. S3 in the Supplemental Material [75] for the $Mn_{3-x}Fe_xSn$ ($x = 0.8$, 1.0, 1.2 and 1.4) compounds. The overall trend aligns well with the XRD results. No phase distortion is observed at low temperatures. The initial refinement using the $\Gamma2$ irreducible representation assumes a simple FM structure with all magnetic moments aligned along the c axis. However, the poor fitting of the (110) reflection peak suggests that the magnetic structure at 5 K is not a simple FM configuration. As show in Fig. S2 in the Supplemental Material [75], the macroscopic magnetization measurements at 5 K reveal a linear magnetization process <1 T, without saturation for fields up to 7 T. This behavior is indicative of the coexistence of FM and AFM contributions. Authors of previous studies also mentioned a coexistence of FM and AFM contributions, which is a common feature in the Mn-Fe-Sn system [58,81–83]. Therefore, in the final refinement, we included two sets of symmetry operations, $\Gamma2$ (FM with moments along the c axis) and $\Gamma8$

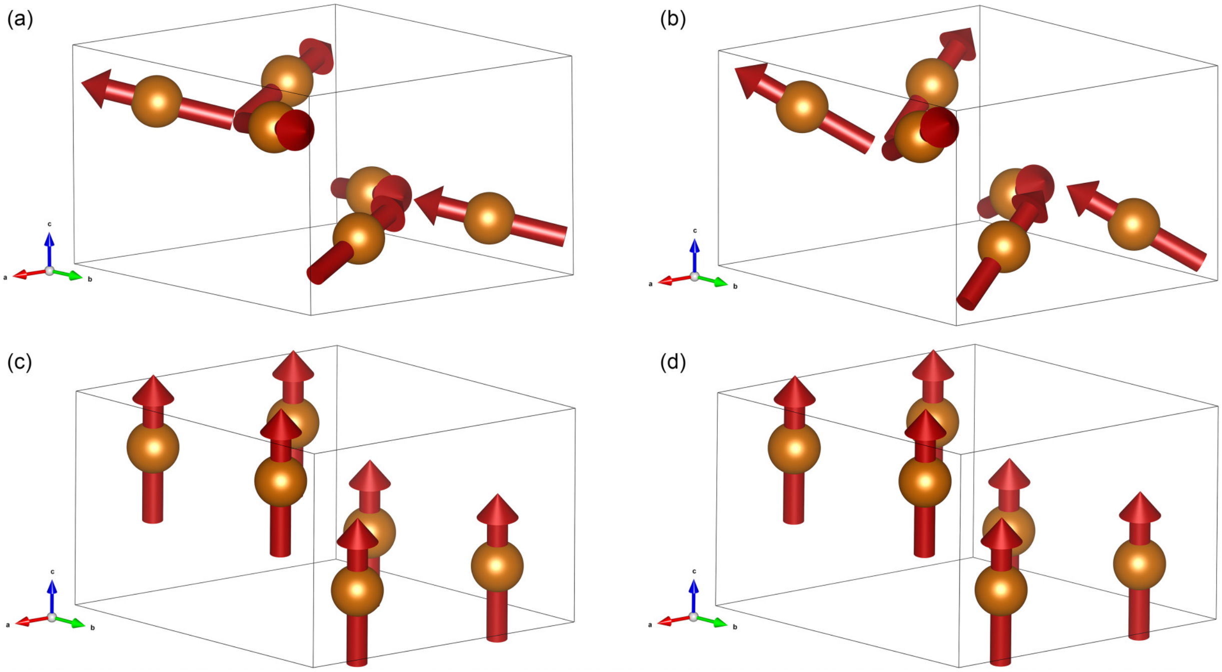

FIG. 5. Low-temperature spin structures of $Mn_{3-x}Fe_xSn$ ($x = 0.8$, 1.0, 1.2, and 1.4) compounds at 5 K. (a) $Mn_{2.2}Fe_{0.8}Sn$, (b) $Mn_{2.0}Fe_{1.0}Sn$, (c) $Mn_{1.8}Fe_{1.2}Sn$, and (d) $Mn_{1.6}Fe_{1.4}Sn$.

(AFM with moments in the $a - b$ plane), to achieve a good fit with the data at 5 and 80 K. For the refinements of ND data at 250 K, we employed the irreducible representation $\Gamma 10$ to describe the FM structure, where the spins are oriented in the $a - b$ plane, as shown in Fig. 4(b) (middle). To validate our hypothesis, we embedded the Mn_2FeSn fine powder in epoxy and aligned the powder particles using a magnetic field of $\mu_0 H = 1$ T during the curing process. Figure 4(c) shows room-temperature XRD measurements of the Mn_2FeSn compound, comparing the field-oriented powder with free powder samples. As a result of the particle orientation in magnetic field, reflections with a pure *a*-axis component, such as (1 0 0) and (2 0 0), are significantly enhanced. Simultaneously, reflections with a pure *c*-axis component, like (0 0 2), vanish almost completely. This indicates that, at room temperature (298 K), the magnetic moments in the Mn_2FeSn compound are aligned within the $a - b$ plane. This observation is consistent with our ND results at 250 K. The hysteresis loops of the field-oriented powders (measured along the field-orientation axis) are shown in Fig. 4(d). At 5 K, the coercive field is $H_C = 25$ mT, and the remnant magnetization is $M_{rem} = 5.22$ $Am^2 kg^{-1}$. At 250 K, we observe soft FM behavior characterized by the absence of hysteresis, which is advantageous for MCM applications. The combined results from ND and oriented powder XRD provide evidence supporting the conclusion that the low-field transition observed at 200 K in the Mn_2FeSn compound corresponds to a spin-reorientation transition (T_S), which is line with a previous study [77]. Below T_S, the Mn_2FeSn compound exhibits coexistence of FM (with spins along the *c* axis) and AFM (with spins in the $a - b$ plane) components, with combined magnetic moments that are oriented out of the basal plane and tilted toward the *c* axis, as shown in Figs. 5(a) and 5(b). Recent calculations by Tagami *et al.* [93] also showed that the out-of-plane canted spin structure has the lowest energy at $x = 0.50$ but becomes metastable at $x = 1.0$. However, above T_S, the compound displays a FM structure aligned within the $a - b$ plane, without any *c*-axis component. Figures 5(a)–5(d) show the refined low-temperature spin structures of $Mn_{3-x}Fe_xSn$ ($x = 0.8$, 1.0, 1.2, and 1.4) compounds at 5 K.

For the $Mn_{3-x}Fe_xSn$ ($x = 1.2$ and 1.4) compounds, ND was carried out at three different temperatures (5, 80, and 500 K). The ND refinement of the $Mn_{1.6}Fe_{1.4}Sn$ pattern is shown in Fig. 6(a). From the comparison of the FM- and PM-state ND patterns, it is evident that the (100) peak exhibits a noticeable magnetic contribution. The magnetic structure was accurately refined using irreducible representation $\Gamma 2$ (FM order with moments along the *c* axis), which is in good agreement with the magnetization saturation behavior observed in Fig. 2(c). To investigate the nature of its magnetocrystalline anisotropy, Fig. 6(b) shows XRD measurements of the $Mn_{1.6}Fe_{1.4}Sn$ compound at room temperature for field-oriented powder and free powder samples. It is clearly seen that reflections with a pure *a*-axis component, like (1 0 0) and (2 0 0), are significantly enhanced. Concurrently, reflections with a pure *c*-axis component, like (0 0 2), disappear completely. This indicates that, at 298 K, the $Mn_{1.6}Fe_{1.4}Sn$ compound exhibits the same spin structure as Mn_2FeSn, where the $a - b$ plane corresponds to the easy magnetization plane, while the *c* axis shows a hard magnetization direction. The magnetic hysteresis loops of the field-oriented powder (along the field-orientation axis) are shown in Fig. S4 in the Supplemental Material [75]. The coercive field is $H_C = 28$ mT, and the remnant magnetization is $M_{rem} = 14.70$ $Am^2 kg^{-1}$ at 5 K.

Figure 7(a) shows the magnetic moment on the 6*h* site per atom for the FM and AFM components obtained from the ND refinement compared with the SQUID

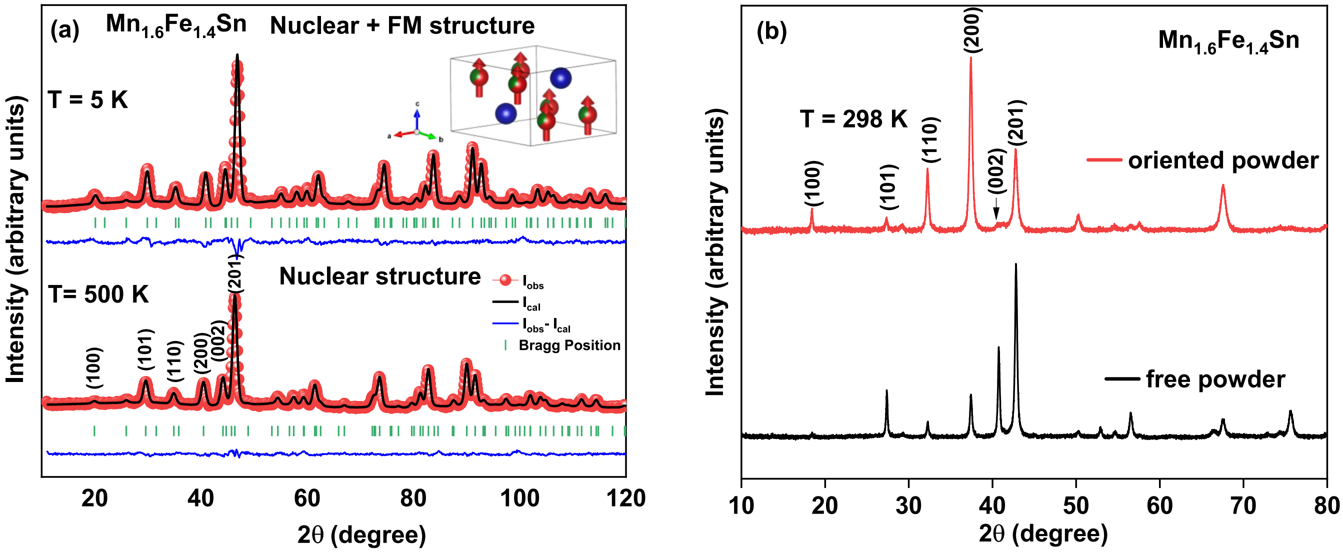

FIG. 6. (a) Refinements of the nuclear and magnetic structure of $Mn_{1.6}Fe_{1.4}Sn$ compound. (b) Comparison between random powder (bottom curve) and field-oriented powder (top curve) x-ray diffraction (XRD) with large changes in the indexed peak intensities.

magnetization results for the $Mn_{3-x}Fe_xSn$ ($x = 0.8$, 1.0, 1.2, and 1.4) compounds. From the ND results, it is found that magnetic moments of the FM component increase from 1.29(7) μ_B/atom ($x = 0.8$) to 1.68(6) μ_B/atom ($x = 1.4$) for increasing Fe content, as listed in Table II. The ND results for the magnetic moments are comparable with the macroscopic magnetization results. For $x = 0.8$ and 1.0, the AFM component shows a larger magnetic moment than the FM component. For the $Mn_{2.2}Fe_{0.8}Sn$ compound at 5 K, the AFM component displays a magnetic moment of 2.23(5) μ_B/atom, consistent with previous polarized neutron experimental studies of pure Mn_3Sn [81]. It is found that the magnetic moment of the AFM component decreases with the Fe concentration. An increasing Fe substitution promotes FM interactions. Additionally, the interatomic distances within a unit cell are essential for determining the structural and electronic properties of a material. These distances, which describe the spacing between atoms in a crystal lattice, are governed by the lattice parameters and the atomic positions within the unit cell. Figure 7(b) shows the interatomic distances of the $Mn_{3-x}Fe_xSn$ ($x = 0.8$, 1.0, 1.2, and 1.4) compounds obtained from refined ND data at different temperatures. It is clearly shown that the intralayer distances gradually decrease with Fe concentration, which is consistent with the trend in lattice parameters. The shortened intralayer metallic-metallic and metallic-metalloid distances will strengthen the $d-d$ hybridization among metallic-metallic atoms and the $p-d$ hybridization among metallic-metalloid atoms due to the increased overlap of electron orbitals [94]. This effect might amplify the magnetic exchange interactions among magnetic atoms. Therefore, the saturation magnetization and transition temperatures increase with increasing Fe contents.

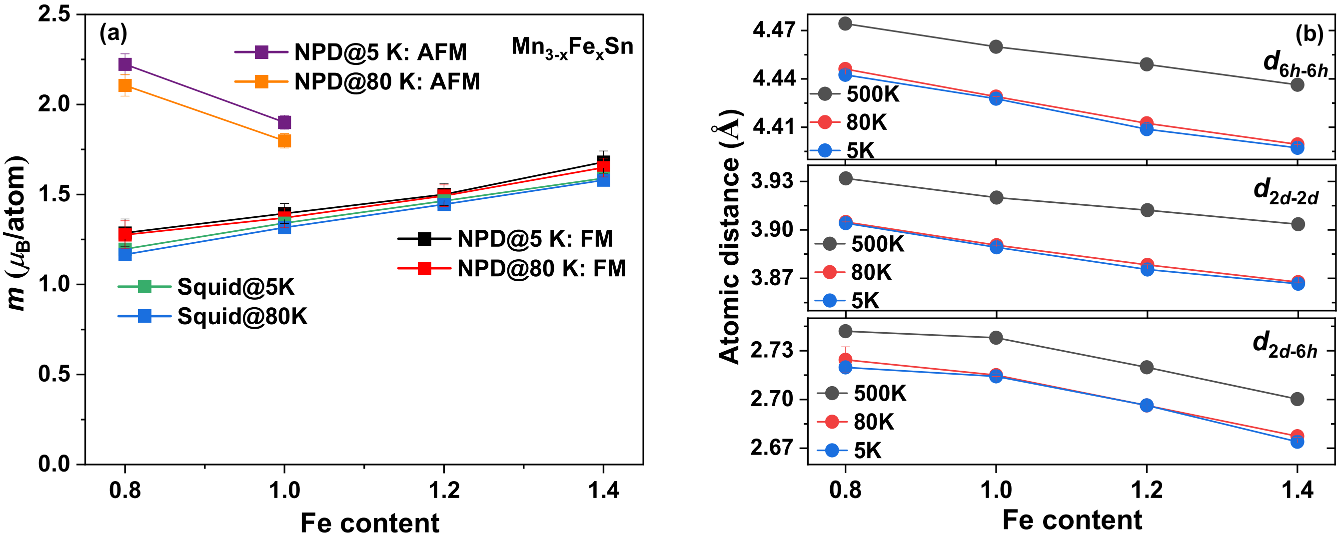

FIG. 7. (a) Magnetic moments for 6*h* site in the hexagonal lattice of the $Mn_{3-x}Fe_xSn$ compounds ($x = 0.8$, 1.0, 1.2, 1.4). (b) Interatomic distances of $Mn_{3-x}Fe_xSn$ compounds ($x = 0.8$, 1.0, 1.2, 1.4) at different temperatures.

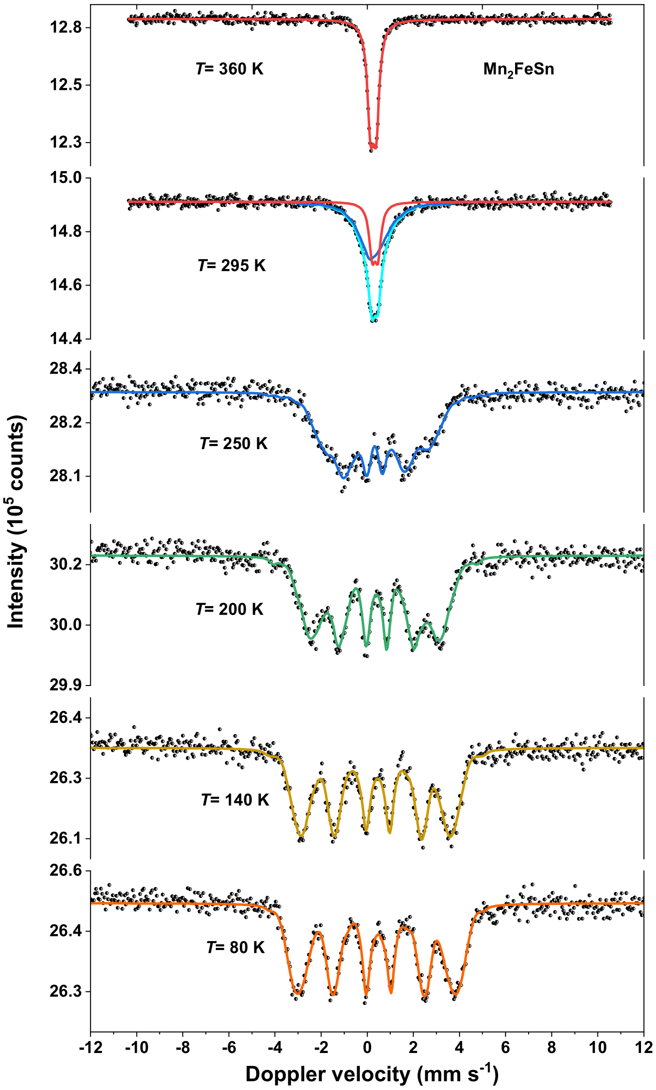

FIG. 8. Mössbauer spectra of the Mn_2FeSn compound at 80, 140, 200, 250, 295, and 360 K. The black points represent the experimental data and colored line is the model fit.

Furthermore, the calculated values at different temperatures show a significant increase in interatomic distances at higher temperatures, indicating thermal expansion due to lattice vibrations.

From the ND results, we determined the spin structure of the magnetic unit cell in the $Mn_{3-x}Fe_xSn$ ($x = 0.8$, 1.0, 1.2, and 1.4) compounds. To investigate the magnetic structure in more detail, we utilized Mössbauer spectroscopy at varying temperatures. Mössbauer spectroscopy plays a crucial role in investigating structural and magnetic phase transitions in magnetic compounds. Figure 8 displays the Mössbauer spectra of the Mn_2FeSn alloy at different temperatures. A good quality of fit to the experimental data is achieved with single-phase models that exhibit small linewidths (0.3 mm/s) for the $6h$ magnetic site, which suggests a homogeneous distribution of the magnetic Fe atoms throughout the Mn_2FeSn compound. At 295 K, the spectrum consists of a sextet magnetic subspectrum and a quadrupole doublet, which is considered the relaxing phase, with coexistence of the FM (69%) and PM (31%) states [52]. This coexistence of FM and PM states is in line with the ND data at 298 K. The temperature dependence of the internal magnetic hyperfine field (B_{hf}) at the $6h$ site is shown in Fig. 9. The compound exhibits $B_{\mathrm{hf}} = 20.54$ T at 5 K, which decreases to $B_{\mathrm{hf}} = 5.42$ T at 295 K. In contrast, the Fe_3Sn compound shows $B_{\mathrm{hf}} = 25.10$ T at the $6h$ site in the hexagonal lattice at room temperature [52]. In numerous publications, it has been noted that the internal magnetic hyperfine field (B_{hf}) and the magnetic moment (μ_{Fe}) show a proportional relation in many Fe-based compounds [95]. However, authors of a recent study have suggested that the measured magnetic moment may not be the primary factor that defines this proportionality; instead, the contribution of the $3d$ moment plays a decisive role. An analysis of the magnetization and the field B_{hf} resulted in a proportionality factor $P = B_{\mathrm{hf}}/\mu_{3d} = 10.37\ \mathrm{T}/\mu_{\mathrm{B}}$ [96]. Employing a proportionality factor of $10.37\ \mathrm{T}/\mu_{\mathrm{B}}$ provides magnetic moments for the Fe ($6h$) site of $\sim 1.98\ \mu_{3d}$/Fe in the Mn_2FeSn compound. The isomer shift and quadrupole splitting are listed in Table III. The isomer shift decreases with increasing temperature due to the second-order Doppler effect. In the Mn_2FeSn compound, the isomer shift decreases by 0.11 mm/s as the temperature increases from 5 to 295 K. A change in quadrupole splitting from negative to positive values is observed across the spin reorientation. This indicates changes in orientation of the local electric field gradient at the nucleus with respect to the spin direction. This reflects a change in the spin-tilt angle across the spin-reorientation transition.

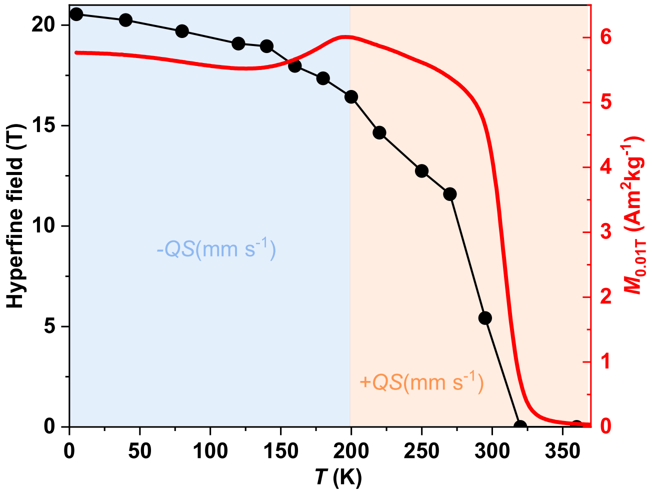

FIG. 9. Temperature dependence of the hyperfine field B_{hf} of the Mn_2FeSn compound, derived from Mössbauer spectroscopy compared with the low-field magnetization in a field of 0.01 T.

D. Electronic and magnetic properties of Mn_2FeSn

The most striking finding of our study is the coexistence of FM and AFM spin structures below T_{S} around the composition Mn_2FeSn. Similar out-of-plane canted spin structures were observed by Tagami *et al.* [93] in a DFT study on $Mn_{3-x}Fe_xSn$ using the VCA around the composition $x = 0.5$. We have also carried out DFT VCA calculations, considering several magnetic orderings: (i) FM $\Gamma 2$ alignment with moments along c, (ii) FM in the $a-b$ plane with moments

TABLE III. Fitted Mössbauer parameters of the Mn_2FeSn compound, obtained at different temperatures. Experimental uncertainties: Isomer shift: IS ± 0.03 $\mathrm{mm\,s^{-1}}$; quadrupole splitting: QS ± 0.03 $\mathrm{mm\,s^{-1}}$; line width: $\Gamma \pm 0.05$ $\mathrm{mm\,s^{-1}}$; hyperfine field: $B_{\mathrm{hf}} \pm 0.2$ T; and spectral contribution: ±3%. FiM: ferrimagnetic state; FM: ferromagnetic state; and PM: paramagnetic state.

Sample	T (K)	IS ($\mathrm{mm\,s^{-1}}$)	QS ($\mathrm{mm\,s^{-1}}$)	Hyperfine field (T)	Γ ($\mathrm{mm\,s^{-1}}$)	Phase
Mn_2FeSn	5	0.45	−0.09	20.54	0.31	FiM
Mn_2FeSn	40	0.47	−0.08	20.25	0.28	FiM
Mn_2FeSn	80	0.45	−0.09	19.7	0.28	FiM
Mn_2FeSn	120	0.43	−0.09	19.08	0.27	FiM
Mn_2FeSn	140	0.42	−0.10	18.95	0.32	FiM
Mn_2FeSn	160	0.40	−0.12	17.97	0.34	FiM
Mn_2FeSn	180	0.39	−0.08	17.35	0.32	FiM
Mn_2FeSn	200	0.38	−0.06	16.43	0.29	FiM
Mn_2FeSn	220	0.38	0.002	14.65	0.36	FM
Mn_2FeSn	250	0.37	0.12	12.74	0.30	FM
Mn_2FeSn	270	0.37	0.08	11.59	0.33	FM
Mn_2FeSn	295	0.28	0.09	5.42	0.32	FM
Mn_2FeSn	295	0.34	0.25	—	0.32	PM
Mn_2FeSn	320	0.29	0.24	—	0.33	PM
Mn_2FeSn	360	0.26	0.24	—	0.32	PM

according Γ10, (iii) $a-b$-plane AFM with Γ8 ordering, and (iv) the specific canted structure, combining Γ2 and Γ8 patterns, that ND reveals for $x = 0.8$ and 1.0 at 5 K [Figs. 5(a) and 5(b)]. In the VCA, Mn and Fe are replaced with a single magnetic species with a fractional core charge determined by x. The results are summarized in Fig. S5 in the Supplemental Material [75]. We find that c-axis FM is most stable for $x \geqslant 0.6$. Indeed, as expected, in the Mn-rich limit ($x \leqslant 0.4$) the a-b-plane AFM ordering is more stable than c-axis FM. Moreover, the c-axis FM (a-b-plane AFM) moment increases (decreases) with x, consistent with the experimental trend. In the crossover region at $x = 0.5$, both the canted and the a-b-plane FM are more stable, where the latter appears to be consistently slightly more stable than the former. This confirms the trend observed by Tagami *et al.* [93]. The trend is also like the ND results; however, where ND has canted moments at $x = 1.0$ in the VCA, the canted structure is unstable at this composition. Moreover, in VCA, the a-b-plane FM ordering is slightly more stable than the canted structure, whereas ND shows canted to be preferred at 5 K. The VCA captures trends, but results are not in quantitative agreement.

To go beyond VCA, we use a supercell Mn_2FeSn with 8 f.u. with Fe and Mn randomly distributed on the $6h$ sublattice. Two magnetic structures were considered: (a) FM, with all moments initialized along c, i.e., like Γ2, and (b) canted, with all moments initialized with the canted ND pattern [Figs. 5(a) and 5(b)]. Details on the moments are summarized in Table IV. The local DOSs are shown in Fig. S6 (Supplemental Material [75]). After optimizing the moments, the FM has retained its collinear ordering along the c axis. However, the size of the average Mn moment is relatively small (2.39 μ_B) and varies strongly from Mn to Mn with a root mean square deviation of 0.6 μ_B. Indeed, the local Mn DOSs are rather dissimilar, as shown in Fig. S6(a) in the Supplemental Material [75].

The canted structure has much lower total energy than c-axis FM: 0.12 eV/f.u. In the canted structure, the moments remain canted, but their orientations exhibit a large degree of disorder, as shown in Fig. 10. The Mn moments are on average larger (2.79 μ_B), and the variation in size has almost disappeared. The local DOSs are also much more similar, and a minimum at the Fermi level has developed, as shown in Figs. S6(d) and S6(e) in the Supplemental Material [75]. The Mn moments pull toward the $a-b$ plane ($\langle\theta_{\mathrm{Mn}}\rangle = 25^\circ$), whereas the Fe moments are much closer to c ($\langle\theta_{\mathrm{Mn}}\rangle = 67^\circ$), i.e., they appear to favor the ordering of their parent compounds ($x = 0$ and 3).

The ND does not resolve the individual magnetic species, i.e., it does not discriminate between Mn and Fe. The average FM (c-axis) moment of 1.38 μ_B can be directly compared and appears to agree well with the ND FM moment of 1.40 μ_B. To enable a rough comparison with the AFM component, we symmetrize the moments with a simple averaging (lattice translations and rotating moments by either 120° or 240°

TABLE IV. Details of the local magnetic moments for the supercell calculations. The average sizes ($\langle m_{\mathrm{Mn}}\rangle$ and $\langle m_{\mathrm{Fe}}\rangle$), the root mean square deviations from the averages (in parentheses), and the average angles of the moments with the ab-plane ($\langle\theta_{\mathrm{Mn}}\rangle$ and $\langle\theta_{\mathrm{Fe}}\rangle$). Symmetrized local moments: size (m), ab-plane component (AFM), and c-axis component (FM).

	Mn		Fe		Symmetrized moments (μ_B)		
	$\langle m_{\mathrm{Mn}}\rangle$ (μ_B)	$\langle\theta_{\mathrm{Mn}}\rangle$	$\langle m_{\mathrm{Fe}}\rangle$ (μ_B)	$\langle\theta_{\mathrm{Fe}}\rangle$	m	m (AFM)	m (FM)
c-axis FM	2.39 (0.58)	87.28°	2.20 (0.15)	88.97°			
Canted	2.79 (0.08)	25.01°	2.11 (0.12)	67.06°	1.979	1.418	1.38
ND at 5 K					2.37	1.91	1.40

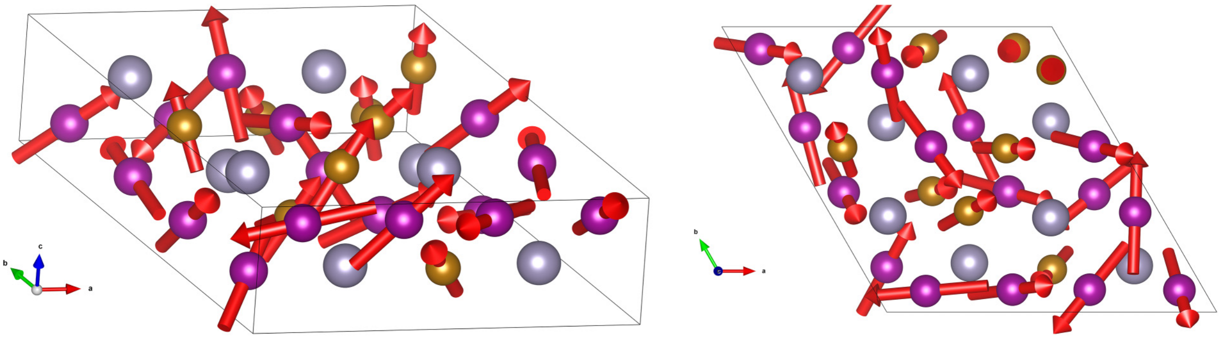

FIG. 10. Magnetic moments in the $Mn_{16}Fe_8Sn_8$ shown from several viewing angles. Picture made with VESTA. Mn purple, Fe gold, and Sn gray spheres [97].

and building the vector sum). The resulting AFM component moment is 1.97 μ_B, to be compared with the ND value of 2.37 μ_B. Given the very small size of the supercell, with only 16 Mn and 8 Fe, averaging might be imperfect. The underestimation could also point to slightly more local order in the material, e.g., by a small tendency for like species to cluster. The Fe local moment (2.10 μ_B) is comparable with the moment estimated from the hyperfine field using the proportionality factor (1.98 μ_B).

IV. CONCLUSIONS

A comprehensive study has been performed to investigate the microstructure, spin structure, and magnetic properties of $Mn_{3-x}Fe_xSn$ ($x = 0.8 - 1.4$) polycrystalline samples. In this study, we have characterized the phase transition, the nature of the magnetic order, and the MCE of the $Mn_{3-x}Fe_xSn$ compounds. We identified the complex spin configuration of the Mn_2FeSn compound, which depends on temperature. A low-temperature transition at T_S is attributed to a spin reorientation. Below T_S, both FM and AFM states coexist and are uniformly distributed. Above T_S, the spin structure rearranges into a FM configuration with spins oriented in the *a-b* plane. However, a new spin model has been derived for the compounds with $x = 1.2$ and 1.4, where a FM component with spins along the *c* axis shows a spin reorientation into an FM structure with spins in the *a-b* plane upon crossing T_S. The magnetic properties were evaluated on random and oriented powders, and an easy plane anisotropy was deduced at room temperature. The Curie temperature T_C, determined by the minimum in dM/dT, ranges from 250 K ($x = 0.8$) to 396 K ($x = 1.4$), highlighting its potential applications for magnetic heat pumps and thermal magnetic motors. Applying Maxwell's relationship to assess the magnetic entropy change, it is found that increasing the iron content up to $x = 1.4$ enhances the magnetic entropy change by 30% compared with $x = 0.8$. DFT calculations of the magnetic moments of Mn and Fe in Mn_2FeSn, as well as the trends in average magnetic moment and unit-cell energy with different Fe concentration, are in good agreement with the present experimental results. This demonstrates that DFT calculations are an effective tool to identify the potential of MCMs and evaluate their magnetic properties in the Mn-Fe-Sn system.

ACKNOWLEDGMENTS

The authors acknowledge Anton Lefering, Bert Zwart, and Robert Dankelman for their technical assistance and Karel Prokeš for valuable contributions and insightful discussions during the ND refinement process. This work is financially supported by the Dutch Research Council NWO TTW with Project No. 17877 and RSP Technology.

DATA AVAILABILITY

The data that support the findings of this article are openly available [98]; embargo periods may apply.

---

[1] P. J. Shamberger and F. S. Ohuchi, Hysteresis of the martensitic phase transition in magnetocaloric-effect Ni-Mn-Sn alloys, Phys. Rev. B **79**, 144407 (2009).

[2] A. Planes, L. Mañosa, and M. Acet, Magnetocaloric effect and its relation to shape-memory properties in ferromagnetic Heusler alloys, J. Phys. Condens. Matter **21**, 233201 (2009).

[3] J. Liu, N. Scheerbaum, S. Kauffmann-Weiss, and O. Gutfleisch, NiMn-based alloys and composites for magnetically controlled dampers and actuators, Adv. Eng. Mater. **14**, 653 (2012).

[4] I. Takeuchi, O. O. Famodu, J. C. Read, M. A. Aronova, K.-S. Chang, C. Craciunescu, S. E. Lofland, M. Wuttig, F. C. Wellstood, L. Knauss *et al.*, Identification of novel compositions of ferromagnetic shape-memory alloys using composition spreads, Nat. Mater. **2**, 180 (2003).

[5] Y. Sutou, Y. Imano, N. Koeda, T. Omori, R. Kainuma, K. Ishida, and K. Oikawa, Magnetic and martensitic transformations of NiMnX (X = In, Sn, Sb) ferromagnetic shape memory alloys, Appl. Phys. Lett. **85**, 4358 (2004).

[6] H. E. Karaca, I. Karaman, B. Basaran, D. C. Lagoudas, Y. I. Chumlyakov, and H. J. Maier, On the stress-assisted magnetic-field-induced phase transformation in Ni_2MnGa ferromagnetic shape memory alloys, Acta Mater. **55**, 4253 (2007).

[7] S. Chadov, X. Qi, J. Kübler, G. H. Fecher, C. Felser, and S. C. Zhang, Tunable multifunctional topological insulators in ternary Heusler compounds, Nat. Mater. **9**, 541 (2010).

[8] R. Weht and W. E. Pickett, Half-metallic ferrimagnetism in Mn_2VAl, Phys. Rev. B **60**, 13006 (1999).

[9] G. D. Liu, X. F. Dai, H. Y. Liu, J. L. Chen, Y. X. Li, G. Xiao, and G. H. Wu, Mn_2CoZ (Z = Al, Ga, In, Si, Ge, Sn, Sb) compounds: Structural, electronic, and magnetic properties, Phys. Rev. B **77**, 014424 (2008).

[10] M. Kratochvílová, D. Král, M. Dušek, J. Valenta, R. H. Colman, O. Heczko, and M. Veis, Fe_2MnSn—Experimental quest for predicted Heusler alloy, J. Magn. Magn. Mater. **501**, 166426 (2020).

[11] B. Dahal, A. Al Maruf, S. Prophet, Y. Huh, P. V. Lukashev, and P. Kharel, Electronic, magnetic, and structural properties of Fe_2MnSn Heusler alloy, AIP Adv. **10**, 015118 (2020).

[12] R. Gauß and O. Gutfleisch, Magnetische Materialien—Schlüsselkomponenten für neue Energietechnologien, in *Rohstoffwirtschaft und Gesellschaftliche Entwicklung*, edited by P. Kausch, J. Matschullat, M. Bertau, and H. Mischo (Springer Spektrum, Berlin, 2016), pp. 99–118.

[13] K. P. Skokov and O. Gutfleisch, Heavy rare earth free, free rare earth and rare earth free magnets—Vision and reality, Scr. Mater. **154**, 289 (2018).

[14] M. R. Felez, A. A. Coelho, and S. Gama, Magnetic properties of $Mn_{3-x}Fe_xSn$ compounds with tuneable Curie temperature by Fe content for thermomagnetic motors, J. Magn. Magn. Mater. **444**, 280 (2017).

[15] T. Jungwirth, X. Marti, P. Wadley, and J. Wunderlich, Antiferromagnetic spintronics, Nat. Nanotechnol. **11**, 231 (2016).

[16] K. Yakushiji, K. Saito, S. Mitani, K. Takanashi, Y. K. Takahashi, and K. Hono, Current-perpendicular-to-plane magnetoresistance in epitaxial $Co_2MnSi/Cr/Co_2MnSi$ trilayers, Appl. Phys. Lett. **88**, 222504 (2006).

[17] C. Felser, G. H. Fecher, and B. Balke, Spintronics: A challenge for materials science and solid-state chemistry, Angew. Chem. Int. Ed. **46**, 668 (2007).

[18] A. Karle, The thermomagnetic Curie-motor for the conversion of heat into mechanical energy, Int. J. Therm. Sci. **40**, 834 (2001).

[19] C. S. Alves, F. C. Colman, G. L. Foleiss, G. T. F. Vieira, and W. Szpak, Numerical simulation and design of a thermomagnetic motor, Appl. Therm. Eng. **61**, 616 (2013).

[20] L. D. R. Ferreira, C. V. X. Bessa, I. Da Silva, and S. Gama, A heat transfer study aiming optimization of magnetic heat exchangers of thermomagnetic motors, Int. J. Refrig. **37**, 209 (2014).

[21] K. Murakami and M. Nemoto, Some experiments and considerations on the behavior of thermomagnetic motors, IEEE Trans. Magn. **8**, 387 (1972).

[22] Y. Takahashi, T. Matsuzawa, and M. Nishikawa, Fundamental performance of the disc-type thermomagnetic engine, Electr. Eng. Jpn. **148**, 26 (2004).

[23] C. S. Alves, F. C. Colman, G. L. Foleiss, W. Szpak, G. T. F. Vieira, and A. C. Bento, Simulation of solar Curie wheel using NiFe alloy and Gd, Int. J. Refrig. **37**, 215 (2014).

[24] Y. W. Yin, M. Raju, W. J. Hu, J. D. Burton, Y.-M. Kim, A. Y. Borisevich, S. J. Pennycook, S. M. Yang, T. W. Noh, A. Gruverman *et al.*, Multiferroic tunnel junctions and ferroelectric control of magnetic state at interface (invited), J. Appl. Phys. **117**, 172601 (2015).

[25] E. Krén, J. Paitz, G. Zimmer, and É. Zsoldos, Study of the magnetic phase transformation in the Mn_3Sn phase, Phys. B+C **80**, 226 (1975).

[26] Y. Liu, B. Zhou, C. Wu, H. Peng, J. Wang, and X. Su, Experimental investigation of the isothermal section of the Fe-Mn-Sn system at 723 K, J. Phase Equilibria Diffus. **39**, 280 (2018).

[27] B. Fayyazi, K. P. Skokov, T. Faske, I. Opahle, M. Duerrschnabel, T. Helbig, I. Soldatov, U. Rohrmann, L. Molina-Luna, K. Güth *et al.*, Experimental and computational analysis of binary Fe-Sn ferromagnetic compounds, Acta Mater. **180**, 126 (2019).

[28] B. Fayyazi, K. P. Skokov, T. Faske, D. Y. Karpenkov, W. Donner, and O. Gutfleisch, Bulk combinatorial analysis for searching new rare-earth free permanent magnets: Reactive crucible melting applied to the Fe-Sn binary system, Acta Mater. **141**, 434 (2017).

[29] M. F. J. Boeije, L. Van Eijck, N. H. Van Dijk, and E. Brück, Structural and magnetic properties of hexagonal $(Mn, Fe)_{3-\delta}Ga$, J. Magn. Magn. Mater. **433**, 297 (2017).

[30] N. H. Sung, F. Ronning, J. D. Thompson, and E. D. Bauer, Magnetic phase dependence of the anomalous Hall effect in Mn_3Sn single crystals, Appl. Phys. Lett. **112**, 132406 (2018).

[31] G. J. Zimmer, E. Kren, C. D. Graham, and J. J. Rhyne, Investigation of the magnetic phase transformation in Mn_3Sn, AIP Conf. Proc. **5**, 513 (1972).

[32] G. J. Zimmer, E. Krén, H. C. Wolfe, C. D. Graham, and J. J. Rhyne, Magnetic structure of DO_{19} type compounds, AIP Conf. Proc. **10**, 1379 (1973).

[33] H. Ohmori, S. Tomiyoshi, H. Yamauchi, and H. Yamamoto, Spin structure and weak ferromagnetism of Mn_3Sn, J. Magn. Magn. Mater. **70**, 249 (1987).

[34] J. Sticht, K.-H. Höck, and J. Kübler, Non-collinear itinerant magnetism: The case of Mn_3Sn, J. Phys. Condens. Matter **1**, 8155 (1989).

[35] P. J. Brown, V. Nunez, F. Tasset, J. B. Forsyth, and P. Radhakrishna, Determination of the magnetic structure of Mn_3Sn using generalized neutron polarization analysis, J. Phys. Condens. Matter **2**, 9409 (1990).

[36] P. Radhakrishna and J. W. Cable, Magnetic excitations in the triangular antiferromagnet Mn_3Sn, J. Magn. Magn. Mater. **104**, 1065 (1992).

[37] J. W. Cable, N. Wakabayashi, and P. Radhakrishna, A neutron study of the magnetic structure of Mn_3Sn, Solid State Commun. **88**, 161 (1993).

[38] J. W. Cable, N. Wakabayashi, and P. Radhakrishna, Magnetic excitations in the triangular antiferromagnets Mn_3Sn and Mn_3Ge, Phys. Rev. B **48**, 6159 (1993).

[39] F. Weitzer and P. Rogl, The Mn-Nd-Sn system (manganese-neodymium-tin), J. Phase Equilibria **14**, 676 (1993).

[40] W. J. Feng, D. Li, W. J. Ren, Y. B. Li, W. F. Li, J. Li, Y. Q. Zhang, and Z. D. Zhang, Glassy ferromagnetism in Ni_3Sn-type $Mn_{3.1}Sn_{0.9}$, Phys. Rev. B **73**, 205105 (2006).

[41] D. Zhang, B. Yan, S.-C. Wu, J. Kübler, G. Kreiner, S. S. P. Parkin, and C. Felser, First-principles study of the structural stability of cubic, tetragonal and hexagonal phases in Mn_3Z (Z = Ga, Sn and Ge) Heusler compounds, J. Phys. Condens. Matter **25**, 206006 (2013).

[42] T. F. Duan, W. J. Ren, W. L. Liu, S. J. Li, W. Liu, and Z. D. Zhang, Magnetic anisotropy of single-crystalline Mn_3Sn in triangular and helix-phase states, Appl. Phys. Lett. **107**, 082403 (2015).

[43] S. Nakatsuji, N. Kiyohara, and T. Higo, Large anomalous Hall effect in a non-collinear antiferromagnet at room temperature, Nature (London) **527**, 212 (2015).

[44] Y. Taguchi, Y. Oohara, H. Yoshizawa, N. Nagaosa, and Y. Tokura, Spin chirality, Berry phase, and anomalous Hall effect in a frustrated ferromagnet, Science **291**, 2573 (2001).

[45] V. Baltz, A. Manchon, M. Tsoi, T. Moriyama, T. Ono, and Y. Tserkovnyak, Antiferromagnetic spintronics, Rev. Mod. Phys. **90**, 015005 (2018).

[46] S. Tomiyoshi and Y. Yamaguchi, Magnetic structure and weak ferromagnetism of Mn_3Sn studied by polarized neutron diffraction, J. Phys. Soc. Jpn. **51**, 2478 (1982).

[47] M. Singh and S. Bhan, Contribution to the Fe-Sn system, J. Mater. Sci. Lett. **5**, 733 (1986).

[48] C. W. Pan, M. P. Hung, and Y. H. Chang, Magnetic properties of mechanically alloyed Fe_3Sn, Mater. Sci. Eng. A **185** 147 (1994).

[49] B. C. Sales, B. Saparov, M. A. McGuire, D. J. Singh, and D. S. Parker, Ferromagnetism of Fe_3Sn and alloys, Sci. Rep. **4**, 7024 (2014).

[50] G. Trumpy, E. Both, C. Djéga-Mariadassou, and P. Lecocq, Mössbauer-effect studies of iron-tin alloys, Phys. Rev. B **2**, 3477 (1970).

[51] H. Giefers and M. Nicol, High pressure x-ray diffraction study of all Fe-Sn intermetallic compounds and one Fe-Sn solid solution, J. Alloys Compd. **422**, 132 (2006).

[52] C. Echevarria-Bonet, N. Iglesias, J. S. Garitaonandia, D. Salazar, G. C. Hadjipanayis, and J. M. Barandiaran, Structural and magnetic properties of hexagonal Fe_3Sn prepared by non-equilibrium techniques, J. Alloys Compd. **769**, 843 (2018).

[53] A. Low, S. Ghosh, S. Changdar, S. Routh, S. Purwar, and S. Thirupathaiah, Tuning of topological properties in the strongly correlated antiferromagnet Mn_3Sn via Fe doping, Phys. Rev. B **106**, 144429 (2022).

[54] O. Yu. Vekilova, B. Fayyazi, K. P. Skokov, O. Gutfleisch, C. Echevarria-Bonet, J. M. Barandiarán, A. Kovacs, J. Fischbacher, T. Schrefl, O. Eriksson *et al.*, Tuning the magnetocrystalline anisotropy of Fe_3Sn by alloying, Phys. Rev. B **99**, 024421 (2019).

[55] Y. Song, Y. Hao, S. Wang, J. Zhang, Q. Huang, X. Xing, and J. Chen, Complicated magnetic structure and its strong correlation with the anomalous Hall effect in Mn_3Sn, Phys. Rev. B **101**, 144422 (2020).

[56] E. Krén and G. Kádár, Neutron diffraction study of Mn_3Ga, Solid State Commun. **8**, 1653 (1970).

[57] S. Tomiyoshi, Polarized neutron diffraction study of the spin structure of Mn_3Sn, J. Phys. Soc. Jpn. **51**, 803 (1982).

[58] J. Liu, S. Zuo, X. Zheng, Y. Zhang, T. Zhao, F. Hu, J. Sun, and B. Shen, Magnetic transition behavior and large topological Hall effect in hexagonal $Mn_{2-x}Fe_{1+x}Sn$ ($x = 0.1$) magnet, Appl. Phys. Lett. **117**, 052407 (2020).

[59] J. Liu, S. L. Zuo, J. Shen, Y. Zhang, Y. Zhang, Z. X. Li, X. Q. Gao, H. F. Kang, T. Y. Zhao, F. X. Hu *et al.*, Large topological Hall effect and *in situ* observation of magnetic domain structures in the Mn_2FeSn compound, Mater. Today Phys. **29**, 100871 (2022).

[60] L. Van Eijck, L. D. Cussen, G. J. Sykora, E. M. Schooneveld, N. J. Rhodes, A. A. Van Well, and C. Pappas, Design and performance of a novel neutron powder diffractometer: PEARL at TU Delft, J. Appl. Crystallogr. **49**, 1398 (2016).

[61] H. M. Rietveld, A profile refinement method for nuclear and magnetic structures, J. Appl. Crystallogr. **2**, 65 (1969).

[62] J. Rodríguez-Carvajal, Recent advances in magnetic structure determination by neutron powder diffraction, Phys. B Condens. Matter **192**, 55 (1993).

[63] Z. Klencsár, Mössbauer spectrum analysis by Evolution Algorithm, Nucl. Instrum. Methods Phys. Res. B. **129**, 527 (1997).

[64] G. Kresse and J. Furthmüller, Efficient iterative schemes for *ab initio* total-energy calculations using a plane-wave basis set, Phys. Rev. B **54**, 11169 (1996).

[65] J. P. Perdew, K. Burke, and M. Ernzerhof, Generalized gradient approximation made simple, Phys. Rev. Lett. **77**, 3865 (1996).

[66] J. P. Perdew, K. Burke, and M. Ernzerhof, Generalized gradient approximation made simple [Phys. Rev. Lett. 77, 3865 (1996)], Phys. Rev. Lett. **78**, 1396(E) (1997).

[67] M. Methfessel and A. T. Paxton, High-precision sampling for Brillouin-zone integration in metals, Phys. Rev. B **40**, 3616 (1989).

[68] G. Kresse and D. Joubert, From ultrasoft pseudopotentials to the projector augmented-wave method, Phys. Rev. B **59**, 1758 (1999).

[69] P. E. Blöchl, Projector augmented-wave method, Phys. Rev. B **50**, 17953 (1994).

[70] D. Hobbs, G. Kresse, and J. Hafner, Fully unconstrained noncollinear magnetism within the projector augmented-wave method, Phys. Rev. B **62**, 11556 (2000).

[71] S. Steiner, S. Khmelevskyi, M. Marsmann, and G. Kresse, Calculation of the magnetic anisotropy with projected-augmented-wave methodology and the case study of disordered $Fe_{1-x}Co_x$ alloys, Phys. Rev. B **93**, 224425 (2016).

[72] P. E. Blöchl, O. Jepsen, and O. K. Andersen, Improved tetrahedron method for Brillouin-zone integrations, Phys. Rev. B **49**, 16223 (1994).

[73] L. Cho, M. S. Kim, Y. H. Kim, and B. C. De Cooman, Influence of minor alloying elements on selective oxidation and reactive wetting of CMnSi TRIP steel during hot dip galvanizing, Metall. Mater. Trans. A **45**, 4484 (2014).

[74] L. Cho, E. J. Seo, G. S. Jung, D. W. Suh, and B. C. De Cooman, Surface selective oxidation of Sn-added CMnSi TRIP steel, Metall. Mater. Trans. A **47**, 1705 (2016).

[75] See Supplemental Material at http://link.aps.org/supplemental/10.1103/pvjm-jvsr for details of the microstructural characterization; magnetization response measured in magnetic fields up to 7 T; structural parameters derived from 5 K ND; results of the irreducible representation analysis based on the hexagonal $P6_3/mmc$ symmetry; VCA-DFT calculations of magnetic and electronic properties as a function of Fe content; and site-projected DOS analysis for $Mn_{16}Fe_8Sn_8$ supercells with random Mn/Fe site occupations.

[76] J. M. Sosa, D. E. Huber, B. Welk, and H. L. Fraser, Development and application of MIPAR^{TM}: A novel software package for two- and three-dimensional microstructural characterization, Integrating Mater. Manuf. Innov. **3**, 123 (2014).

[77] T. Ghosh, S. Agarwal, and P. K. Mukhopadhyay, Structural and magnetic properties of $Mn_{50}Fe_{50-x}Sn_x$ ($x = 10$, 15 and 20) alloys, J. Magn. Magn. Mater. **418**, 260 (2016).

[78] Y. Yang, Z. Li, Z. Li, J. Yang, B. Yang, Y. Dong, H. Yan, Y. Zhang, C. Esling, X. Zhao, and L. Zuo, Microstructural feature

and magnetocaloric effect of $Mn_{50}Ni_{40.5}In_{9.5}$ melt-spun ribbons, Crystals **7**, 289 (2017).

[79] J. Guo, M. Zhong, W. Zhou, Y. Zhang, Z. Wu, Y. Li, J. Zhang, Y. Liu, and H. Yang, Grain size effect of the γ phase precipitation on martensitic transformation and mechanical properties of Ni–Mn–Sn–Fe Heusler alloys, Materials **14**, 2339 (2021).

[80] F. Zhang, K. Westra, Q. Shen, I. Batashev, A. Kiecana, N. Van Dijk, and E. Brück, The second-order magnetic phase transition and magnetocaloric effect in all-d-metal NiCoMnTi-based Heusler alloys, J. Alloys Compd. **906**, 164337 (2022).

[81] T. Hori, H. Niida, Y. Yamaguchi, H. Kato, and Y. Nakagawa, Antiferromagnetic to ferromagnetic transition of DO_{19} type $(Mn_{1-x}Fe_x)_3Sn_{1-\delta}$, J. Magn. Magn. Mater. **90**, 159 (1990).

[82] X. Q. Zheng, X. P. Shao, J. Chen, Z. Y. Xu, F. X. Hu, J. R. Sun, and B. G. Shen, Giant magnetocaloric effect in $Ho_{12}Co_7$ compound, Appl. Phys. Lett. **102**, 022421 (2013).

[83] P. K. Rout, P. V. P. Madduri, S. K. Manna, and A. K. Nayak, Field-induced topological Hall effect in the noncoplanar triangular antiferromagnetic geometry of Mn_3Sn, Phys. Rev. B **99**, 094430 (2019).

[84] T. Gottschall, K. P. Skokov, M. Fries, A. Taubel, I. Radulov, F. Scheibel, D. Benke, S. Riegg, and O. Gutfleisch, Making a cool choice: The materials library of magnetic refrigeration, Adv. Energy Mater. **9**, 1901322 (2019).

[85] W. Hanggai, O. Tegus, H. Yibole, and F. Guillou, Structural and magnetic phase diagrams of $MnFe_{0.6}Ni_{0.4}$(Si, Ge) alloys and their giant magnetocaloric effect probed by heat capacity measurements, J. Magn. Magn. Mater. **494**, 165785 (2020).

[86] H. Ojiyed, M. van den Berg, I. Batashev, Q. Shen, N. van Dijk, and E. Brück, Magnetocaloric properties of $Mn_5(Si,\ P)B_2$ compounds for energy harvesting applications, J. Alloys Compd. **978**, 173485 (2024).

[87] V. K. Pecharsky and K. A. Gschneidner, Jr., Giant magnetocaloric effect in $Gd_5(Si_2Ge_2)$, Phys. Rev. Lett. **78**, 4494 (1997).

[88] K. A. Gschneidner, Jr., V. K. Pecharsky, and A. O. Tsokol, Recent developments in magnetocaloric materials, Rep. Prog. Phys. **68**, 1479 (2005).

[89] V. K. Pecharsky and K. A. Gschneidner, Jr., Magnetocaloric effect from indirect measurements: Magnetization and heat capacity, J. Appl. Phys. **86**, 565 (1999).

[90] V. Franco, J. S. Blázquez, and A. Conde, Field dependence of the magnetocaloric effect in materials with a second order phase transition: A master curve for the magnetic entropy change, Appl. Phys. Lett. **89**, 222512 (2006).

[91] J. Y. Law, V. Franco, L. M. Moreno-Ramírez, A. Conde, D. Y. Karpenkov, I. Radulov, K. P. Skokov, and O. Gutfleisch, A quantitative criterion for determining the order of magnetic phase transitions using the magnetocaloric effect, Nat. Commun. **9**, 2680 (2018).

[92] N. H. van Dijk, Landau model evaluation of the magnetic entropy change in magnetocaloric materials, J. Magn. Magn. Mater. **529**, 167871 (2021).

[93] K. Tagami, T. Ohno, J. Nara, and M. Usami, Magnetic structures and magnetic anisotropy of $Mn_{3-x}Fe_xSn$ studied by first-principles calculations, Jpn. J. Appl. Phys **63**, 023001 (2024).

[94] R. H. Petrucci, *General Chemistry: Principles and Modern Applications*, 10th ed. (Pearson Prentice Hall, Toronto, 2010).

[95] O. Eriksson and A. Svane, Isomer shifts and hyperfine fields in iron compounds, J. Phys. Condens. Matter **1**, 1589 (1989).

[96] M. Ghafari, H. Hahn, T. Feng, R. Kruk, and M. Yan, On the relationship between magnetic moment and nuclear magnetic hyperfine field of ^{57}Fe, Hyperfine Interact. **242**, 2 (2021).

[97] K. Momma and F. Izumi, VESTA 3 for three-dimensional visualization of crystal, volumetric and morphology data, J. Appl. Crystallogr. **44**, 1272 (2011).

[98] W. Hanggai, O. Hamutu, G. A. de Wijs, I. Dugulan, N. H. van Dijk, and E. Brück, Original experimental data for the paper "Complex spin structure and magnetic phase transition of $Mn_{3-x}Fe_xSn$ Alloys," Version 1. 4TU. ResearchData. Dataset, https://data.4tu.nl/datasets/a8fc2b7d-1cb7-4499-a486-930ff5117f96.